

Fluctuating hydrodynamic modelling of fluids at the nanoscale

G. De Fabritiis,^{1,*} M. Serrano,^{2,†} R. Delgado-Buscalioni,^{3,‡} and P. V. Coveney^{4,§}

¹*Computational Biochemistry and Biophysics Lab (GRIB/IMIM-UPF),
Barcelona Biomedical Research Park (PRBB), C/ Dr. Aiguader 88, 08003, Barcelona, Spain*

²*Depto. Física Fundamental, Facultad de Ciencias,
UNED, Paseo Senda del Rey 9, 28040 Madrid, Spain.*

³*Depto. Ciencias y Técnicas Fisicoquímicas, Facultad de Ciencias,
UNED, Paseo Senda del Rey 9, Madrid 28040, Spain.*

⁴*Centre for Computational Science, Department of Chemistry,
University College London, 20 Gordon Street, WC1H 0AJ London, U.K.*

A good representation of mesoscopic fluids is required to combine with molecular simulations at larger length and time scales (De Fabritiis *et. al*, Phys. Rev. Lett. 97, 134501 (2006)). However, accurate computational models of the hydrodynamics of nanoscale molecular assemblies are lacking, at least in part because of the stochastic character of the underlying fluctuating hydrodynamic equations. Here we derive a finite volume discretization of the compressible isothermal fluctuating hydrodynamic equations over a regular grid in the Eulerian reference system. We apply it to fluids such as argon at arbitrary densities and water under ambient conditions. To that end, molecular dynamics simulations are used to derive the required fluid properties. The equilibrium state of the model is shown to be thermodynamically consistent and correctly reproduces linear hydrodynamics including relaxation of sound and shear modes. We also consider non-equilibrium states involving diffusion and convection in cavities with no-slip boundary conditions.

PACS numbers: 47.61.-k,47.11.Mn

I. INTRODUCTION

From a continuum perspective the fundamental equations underlying hydrodynamics at the mesoscale are the well known fluctuating hydrodynamics (FH) equations [1]. The FH equations are stochastic partial differential equations that reduce to the Navier-Stokes equations in the limit of large volumes. In fact, at scales of nano to micro meters, thermal fluctuations cannot be neglected, but must be incorporated as random terms in the momentum and energy equations of hydrodynamics because they are responsible for the mechanical and thermal energy processes underlying Brownian motion. The hydrodynamics of nanoscopic quantities of liquids, in particular for water models used in molecular dynamics simulations such as TIP3P [2], is relevant in many biological and technological applications.

Novel multiscale modelling techniques via domain decomposition (particle-continuum hybrid approach) require a very accurate description of thermodynamics and hydrodynamics at the mesoscale level [3, 4]. In these methods a large part of the system is resolved with a continuum model (CFD) and a smaller part using full-atom molecular dynamics (MD). An exact match between the local thermodynamic and hydrodynamic properties of the continuum and the molecular system is required for such a scheme to work properly. This matching enables

a seamless coupling such that the behaviour of molecular and hybrid simulations are indistinguishable [4]. Depending on the process or regime being considered fluctuations may play an important rôle [5]. For these reasons, the fluctuating hydrodynamics model described here has been used in the first hybrid MD-FH model for water which includes mass and momentum fluctuations as well as for propagation of sound waves across an hybrid interface [4, 6] because of the need to have a fine control over the characteristics of the fluid to match the molecular description (shear and bulk viscosities, equation of state and thermodynamic fluctuations).

An accurate code for fluctuating hydrodynamics, possibly interfaced with molecular dynamics, would be a useful tool for nanoscale computational fluid dynamics (CFD) simulation, including *inter alia* microfluidic devices [7]. These devices are essentially hydraulic micro machines which are able to process nano liters of reagents. These volumes are too large to be simulated by molecular dynamics, while, on the other hand, a standard CFD code cannot handle fluctuations at all.

A general purpose FH solver could also be used to provide an implicit hydrodynamic solvent for solute particles (polymers, colloids, etc.). Solvent molecules often comprise the computationally most expensive part of any molecular or coarse-grained simulation, but in some instances the solvent could be approximated by an “implicit description”, retaining only the hydrodynamic contribution to the solute dynamics. A possible approach was first illustrated in [8]. A solver of FH for the hydrodynamic description of these hybrid models could be employed to study the effect on polymer collapse of changing solvent characteristics [9] by tuning the characteristics of

*gdefabritiis@imim.es

†mserrano@fisfun.uned.es

‡rafa@ccia.uned.es

§p.v.coveney@ucl.ac.uk

the fluids such as their viscosities.

In recent years, many computational models have been devised which provide a discrete representation of FH [10, 11, 12], e. g. dissipative particle dynamics (DPD) [13, 14] and the lattice Boltzmann method (LBM) [11, 15, 16, 17, 18] later extended to include thermodynamic fluctuations [19, 20, 21]. Following a continuum approach, the fundamental equations of fluctuating hydrodynamics can also be resolved directly via finite differences or finite volume schemes [22, 23]. Most of the previous schemes proposed for solving fluctuating hydrodynamics considered only the gas phase [22, 24] and have focused on the linear regime where a closed set of equations for the fluctuating quantities or for their mutual spatial correlations can be derived [24]. The main difficulty in devising a discretization of the FH equations is that the precise form of the required fluctuation-dissipation relations depends on the discretization scheme and, in general, it does not coincide with the fluctuation-dissipation relations of the continuum description. This statement applies for Lagrangian FH models [23, 25, 26], for fluctuating lattice Boltzmann models [19, 20, 21] and for the Eulerian FH description. Moreover the resulting equations are stochastic in nature which adds extra complications to the integration methods [27, 28, 29].

For these reasons, a simple and easy-to-implement general purpose solver of the compressible FH equations allowing fluid specificity and non-linear hydrodynamic coupling is not readily available. It is the purpose of this paper to address this lacuna. We present a finite volume discretization of the compressible isothermal fluctuating hydrodynamic equations, based on an Eulerian description on a regular grid. The model provides a thermodynamically consistent coarse-grained representation of nano liter portions of real fluids ranging from gases (argon) to liquids (water).

The outline of the paper is the following: The fluctuating hydrodynamic Eulerian solver is described in section II. In section III we study the numerical accuracy of the scheme by comparing the input values of the viscosities with the effective ones measured from the hydrodynamic solver based on the relaxation of sound and shear waves. In section IV we assess the validity of the description of the equilibrium state, showing that fluctuations are correctly generated, propagated and dissipated. To that end we calculate the time correlation functions of the different fluctuating variables of one fluid cell (density and velocity) and compare them with the corresponding grand canonical result. In section V we consider non-equilibrium states in closed systems with rigid walls, using the no-slip boundary condition: we test them for Couette, Poiseuille and cavity flows. Finally, we summarise our findings in section VI.

II. A FINITE VOLUME DISCRETIZATION OF FLUCTUATING HYDRODYNAMICS

Our proposed mesoscopic model is a finite volume discretization of FH [23, 26] over a regular lattice in the Eulerian frame of reference. In this case, we concentrate on the description of an isothermal compressible fluid. This sort of description can be generalized straightforwardly to non-isothermal states for fluids with vanishingly small thermal expansion, for which the energy equation decouples from the mass and momentum equations [22]. Extensions to include energy flows will be considered elsewhere. We thus require the equations of fluctuating hydrodynamics describing the conservation of mass and momentum,

$$\begin{aligned}\partial_t \rho &= -\partial_\beta g_\beta, \\ \partial_t g_\alpha &= -\partial_\beta \left(g_\beta v_\alpha + \Pi_{\alpha\beta} + \tilde{\Pi}_{\alpha\beta} \right),\end{aligned}\quad (1)$$

where $\rho(\mathbf{r}, t)$ is the density field of the fluid, $v_\alpha(\mathbf{r}, t)$ is the continuous velocity field in the component α , $g_\beta(\mathbf{r}, t) = \rho(\mathbf{r}, t)v_\beta(\mathbf{r}, t)$ is the momentum field and we have used the repeated suffix convention for summation over repeated indices. $\Pi_{\alpha\beta}(\mathbf{r}, t)$ and $\tilde{\Pi}_{\alpha\beta}(\mathbf{r}, t)$ are respectively the average (Navier-Stokes) and fluctuating stress tensor fields. The average stress tensor is defined as $\mathbf{\Pi} = (p + \pi)\mathbf{1} + \overline{\mathbf{\Pi}}$, where p is the thermodynamic pressure given by the equation of state for the fluid, $\pi = -\zeta \partial_\gamma v_\gamma$ and $\overline{\Pi}_{\alpha\beta} = -\eta (\partial_\alpha v_\beta + \partial_\beta v_\alpha - 2D^{-1} \partial_\gamma v_\gamma \delta_{\alpha\beta})$ where η and ζ are the shear and bulk viscosity respectively and D is the spatial dimensionality.

The equation of state $p = p(\rho, T)$ for Lennard-Jones (LJ) fluids (like argon) has been studied by several authors (see e.g., Ref. [30]), as well as the transport coefficients of the LJ fluid [31, 32]. By contrast, the equation of state of the TIP3P model for water [2] (chosen due to its importance in biological applications) has received less attention [33]. In Appendix B we provide a parametric study of the equations of state of the fluids considered here (argon and TIP3P water model), performed via molecular dynamics (MD) simulations. From this study we obtain a second order polynomial fit for $p = p(\rho, T)$ which provides the equation of state of our FH model. This procedure is required, for instance, to provide the level of accuracy for the thermodynamic pressure within hybrid MD simulations [4]. We have also calculated the transport coefficients of water via non-equilibrium molecular dynamics, which are in agreement with those reported in the literature [34].

The fluctuating stress tensor $\tilde{\Pi}_{\alpha\beta}$ (see Ref.[1]) is a random Gaussian matrix with zero mean and correlations given by

$$\langle \tilde{\Pi}_{\alpha\beta}(\mathbf{r}_1, t_1) \tilde{\Pi}_{\delta\gamma}(\mathbf{r}_2, t_2) \rangle = 2k_B T C_{\alpha\beta\gamma\delta} \delta(t_1 - t_2) \delta(\mathbf{r}_1 - \mathbf{r}_2), \quad (2)$$

where $C_{\alpha\beta\gamma\delta} = [\eta(\delta_{\alpha\delta}\delta_{\beta\gamma} + \delta_{\alpha\gamma}\delta_{\beta\delta}) + (\zeta - \frac{2}{D}\eta)\delta_{\alpha\beta}\delta_{\delta\gamma}]$, k_B is the Boltzmann constant and T is the temperature.

Note that this spatial delta-correlated quantity, in the discrete limit of a small volume and small time interval, can be rewritten as

$$\langle \tilde{\Pi}_{\alpha\beta}(\mathbf{r}_1, t_1) \tilde{\Pi}_{\delta\gamma}(\mathbf{r}_2, t_2) \rangle \approx \frac{2k_B T}{\Delta t \Delta V} C_{\alpha\beta\gamma\delta}, \quad (3)$$

where ΔV is the small volume element of fluid and Δt is the time step.

The fluctuating hydrodynamic equations (1) are balance equations of the form $\partial_t \phi(\mathbf{r}, t) = -\nabla \cdot \mathbf{J}^\phi$ for mass and momentum which can be integrated by considering a finite volume discretization. In what follows we will derive a finite volume discretization of the equations of fluctuating hydrodynamics in the Eulerian system of reference. We first partition the space into N space filling volumes V_k (in our case a regular Cartesian lattice is used) with $k = 1, \dots, N$ to integrate Eqs. (1) over the volume V_k and apply Gauss's theorem

$$\frac{d}{dt} \int_{V_k} \phi(\mathbf{r}, t) d\mathbf{r} = \sum_l \mathbf{J}_{kl}^\phi \cdot \mathbf{e}_{kl} A_{kl}, \quad (4)$$

where \mathbf{e}_{kl} is the unit vector perpendicular to the contact surface of area A_{kl} from volume l to volume k . The summation is over all the l volumes that are in contact with fluid volume k . By defining $M_k^t = \int_{V_k} \rho(\mathbf{r}, t) d\mathbf{r}$ as the mass inside a generic volume V_k , and $\mathbf{P}_k^t = \int_{V_k} \rho(\mathbf{r}, t) \mathbf{v}(\mathbf{r}, t) d\mathbf{r}$ its momentum, we thus build dynamical equations corresponding to discrete extensive variables which replace Eqs.(1) governing the time evolution of the intensive continuum fields. These new equations are given by

$$\begin{aligned} dM_k^t &= \sum_l \mathbf{g}_{kl} \cdot \mathbf{e}_{kl} A_{kl} dt, \\ d\mathbf{P}_k^t &= \sum_l (\mathbf{v}_{kl} \mathbf{g}_{kl} + \mathbf{\Pi}_{kl}) \cdot \mathbf{e}_{kl} A_{kl} dt + d\tilde{\mathbf{P}}_k^t, \end{aligned} \quad (5)$$

where we have approximated the mass flux \mathbf{J}_{kl}^ρ with $\mathbf{g}_{kl} = \frac{1}{2}(\rho_k + \rho_l) \frac{1}{2}(\mathbf{v}_k + \mathbf{v}_l)$, the velocity on the surface kl as $\mathbf{v}_{kl} = \frac{1}{2}(\mathbf{v}_k + \mathbf{v}_l)$, the average stress tensor on the surface as $\mathbf{\Pi}_{kl} = \frac{1}{2}[(p_l + p_k) \mathbf{1} + \bar{\mathbf{\Pi}}_l]$ and $d\tilde{\mathbf{P}}_k^t$ indicates the momentum change due to the fluctuating part of the pressure tensor, all at time t .

An essential component for the discretization of a stochastic mesoscopic model is the balancing of dissipative and fluctuating components, otherwise the fluctuation-dissipation theorem would not be satisfied. There are at least two ways to satisfy this condition, either by using the Fokker-Planck equations mathematically equivalent to the stochastic differential equations (SDE 5) and equating dissipative and diffusive terms weighted over the Gibbs ensemble distribution [26] or by using the GENERIC formalism [23, 35]. By choosing the gradient discretization provided in [23] a lot of

long algebra is avoided; we find discrete versions for

$$\begin{aligned} \bar{\Pi}_k^{\alpha\beta} &= \frac{\eta_k}{V_k} \sum_l \left[\frac{A_{kl}}{2} (e_{kl}^\alpha v_l^\beta + e_{kl}^\beta v_l^\alpha) - \frac{\delta^{\alpha\beta}}{D} A_{kl} e_{kl}^\gamma v_l^\gamma \right], \\ \pi_k &= \frac{\zeta_k}{V_k} \sum_l \frac{A_{kl}}{2} e_{kl}^\beta v_l^\beta, \end{aligned} \quad (6)$$

and the fluctuating component of the momentum equation given by

$$\begin{aligned} d\tilde{\mathbf{P}}_k^t &= \sum_l \frac{A_{kl}}{2} \sqrt{4k_B T_l \frac{\eta_l}{V_l}} d\bar{\mathbf{W}}_l^S \cdot \mathbf{e}_{kl} \\ &+ \sum_l \frac{A_{kl}}{2} \sqrt{2Dk_B T_l \frac{\zeta_l}{V_l}} \frac{tr[d\mathbf{W}_l]}{D} \mathbf{e}_{kl}, \end{aligned} \quad (7)$$

where $d\mathbf{W}_l$ is a $D \times D$ matrix ($D = 3$ in three dimensions) of independent Wiener increments satisfying $\langle d\mathbf{W}_k^{\alpha\beta} d\mathbf{W}_l^{\gamma\delta} \rangle = \delta_{kl} \delta_{\alpha\gamma} \delta_{\beta\delta} dt$ and $d\bar{\mathbf{W}}_l^S$ is a traceless symmetric random matrix defined as

$$d\bar{\mathbf{W}}_l^S = \frac{(d\mathbf{W}_l + d\mathbf{W}_l^T)}{2} - \frac{tr[d\mathbf{W}_l]}{D} \mathbf{1}. \quad (8)$$

The resulting set of stochastic differential equations is integrated using a simple stochastic Euler scheme in the present work. Note, however, that other more accurate stochastic integration schemes for mesoscopic models have recently been proposed based on the Trotter expansion in the stochastic case [28, 29]. Improvements to the solver for the spatial regular grid and for the time integration scheme have not been considered for the present scheme because at these scales the Reynolds number is usually low and the computational limitation comes rather from the molecular dynamics component. However, generalizations to unstructured grids are straightforward. In particular, in a hybrid MD-CFD model finer cells should be located near the MD region and coarser, bigger cells further away from the MD domain.

III. ACCURACY OF THE SCHEME

To assess the accuracy of the numerical scheme, we measure the effective viscosities and sound velocity computed from the hydrodynamic solver and compare them with the input values. The transport coefficients are measured from the relaxation of transversal and longitudinal waves in the deterministic limit. We give more details in Appendix A. In the following tests we consider argon at temperature $T = 300$ K and mass equilibrium density $\rho_e = 0.6$ g/mol/ \AA^3 and TIP3P water. The corresponding values of the dynamic shear and bulk viscosity for argon and water are shown in table I, along with the isothermal sound velocity, $c_T^2 \equiv (\partial P / \partial \rho)_T$ and sound absorption coefficient Γ_T . We consider a periodic 3D cubic domain of length L ; thus, the permitted wavelengths are $k_n = 2\pi n / L$, and we excite the longest wavelength of the system, of wave-number $2\pi / L$.

TABLE I: Some properties of argon and water at $T = 300$ K at the mass densities ρ considered; m is the molecular mass. Note that length, time and mass units are \AA , ps and g/mol respectively. The properties displayed are shear viscosity (η), bulk viscosity (ζ), isothermal sound speed (c_T) and isothermal sound absorption (Γ_T) in corresponding units.

liquid	m	ρ	η	ζ	c_T	Γ_T
argon	39.948	0.60	5.474	1.823	5.614	7.612
water	18.015	0.632	53.71	127.05	14.75	157.17

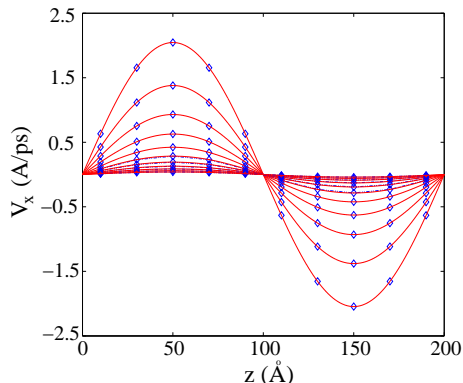


FIG. 1: Velocity field v_x as a function of z (in \AA) for this decaying transversal wave. Diamonds correspond to simulation results and the continuum lines correspond to the theoretical profile at snapshots corresponding to times $t = 0, 50, 100, \dots, 750$ ps. At time $t = 0$ ps the amplitude is maximum while at $t = 750$ ps the amplitude is minimum.

A. Transversal wave

The wave-vector of a transversal wave is perpendicular to its velocity, $\mathbf{k} \perp \mathbf{v}$. Consider an initial perturbative velocity $\mathbf{v} = (v_0 \sin(kz), 0, 0)$, with $\mathbf{k} = (0, 0, k)$. For small perturbations around equilibrium, the linearized solution for the momentum density field in Fourier space given in Eqs.(A9) is

$$\mathbf{g}(\mathbf{k}, t) = \exp\{-\nu k^2 t\} \mathbf{g}(\mathbf{k}, 0), \quad (9)$$

while in real space, the time dependent velocity field reads

$$v_x(t) = v_0 \sin(kz) \exp\{-\nu k^2 t\}; \quad (10)$$

in addition $v_y(t) = v_z(t) = 0$ and $\rho(t) = \rho_e$.

In Fig.1 we plot some snapshots of the velocity field for a deterministic simulation. This case represents a three dimensional simulation box of $200 \times 200 \times 200 \text{\AA}^3$ ($10 \times 10 \times 10$ cells) which corresponds to a spatial resolution $\delta = 20 \text{\AA}$. The applied initial velocity amplitude is $v_0 = 2.04 \text{\AA}/\text{ps}$, the argon input viscosity at 300 K is $\eta = 5.4744$ and the mean mass density is $\rho = 0.6 \text{ g/mol}/\text{\AA}^3$. The theoretical agreement with expression (10) is remarkable.

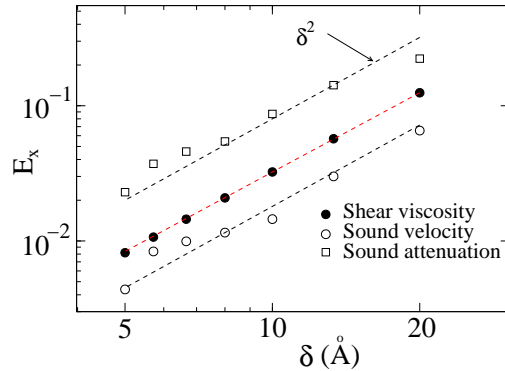


FIG. 2: Relative error for the shear viscosity, sound absorption coefficient and sound velocity as a function of the spatial resolution δ . For any fluid parameter (e.g. ν) the relative error is defined as $E_\nu \equiv |\nu_{num} - \nu|/\nu$, where ν is the input value and ν_{num} that measured from the relaxation of the corresponding hydrodynamic mode.

For a closer inspection of the numerical accuracy of the scheme we compared the effective (or numerical) shear viscosity ν_{num} with the input value ν . The value of ν_{num} was measured by fitting the decay of the Fourier component of the transversal momentum to a simple exponential function. The relative error in viscosity $E_\nu \equiv |\nu_{num} - \nu|/\nu$ is shown in Fig.2 against the spatial resolution δ , given by the distance between contiguous cells. The trend obtained is $E_\nu \propto \delta^{-1.94}$, showing that our spatial discretization method is of second order. As an example, a continuum cell size of $\delta = 20 \text{\AA}$ will give an error in the viscosity around 12% while $\delta = 15 \text{\AA}$ will reduce the relative error to 5% for the perturbation applied here.

B. Longitudinal wave

If the equilibrium state of the fluid is initially perturbed with a momentum field $\mathbf{g}_0 = (g_0 \sin kx, 0, 0)$, a longitudinal sound wave is created with a wave-vector parallel to the momentum perturbation $\mathbf{k} = (2\pi/L, 0, 0)$. As shown in Appendix A, two travelling sound modes propagate at the sound velocity c_T , creating a standing wave in the periodic domain. According to Eqs. (A9) the Fourier components of the deviation from the equilibrium state for the density and velocity of the sound modes are given by

$$\begin{aligned} \delta\rho(\mathbf{k}, t) &\propto -i \exp\{-\Gamma_T k^2 t\} \sin(c_T k t) \frac{\mathbf{k} \cdot \mathbf{g}_0}{c_T}, \\ \delta\mathbf{g}(\mathbf{k}, t) &\propto \exp\{-\Gamma_T k^2 t\} \cos(c_T k t) \mathbf{k} \frac{\mathbf{k} \cdot \mathbf{g}_0}{c_T}, \end{aligned} \quad (11)$$

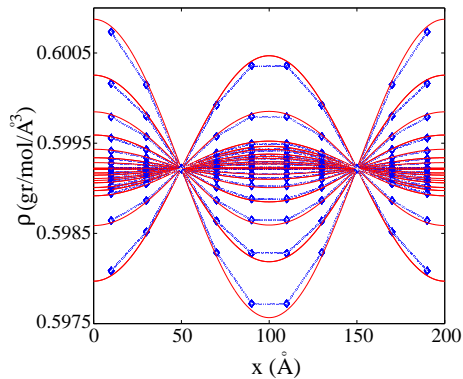


FIG. 3: The mass density ρ as a function of x (in \AA) for a decaying longitudinal wave. Diamonds correspond to simulation results and the continuum lines correspond to the theoretical profile given by Eq. (12). The snapshots correspond to the times $t = 0, 25, 50, \dots, 750$ ps. The agreement is remarkable. At time $t = 0$ ps the amplitude is maximum while at $t = 750$ ps the amplitude is minimum.

while in real space the density and velocity fields evolve like

$$\begin{aligned}\rho(t) &= \rho_e + \frac{g_0}{c_T} \cos(kx) \sin(c_T k t) \exp\{-\Gamma_T k^2 t\}, \\ v_x(t) &= \frac{g_0}{\rho_e} \sin(kx) \cos(c_T k t) \exp\{-\Gamma_T k^2 t\}\end{aligned}\quad (12)$$

and the other velocity field components remain at rest. Note that ρ_e denotes the equilibrium density.

In Fig.3 we plot the density field as a function of x for a deterministic three dimensional simulation of size $200 \times 200 \times 200 \text{ \AA}^3$ ($10 \times 10 \times 10$ cells). In order to keep the system in the linear regime, the applied initial velocity amplitude is set to $v_0 = 0.0204 \text{ \AA/ps}$ and the argon input mean mass density is $\rho = 0.6 \text{ g/mol/\AA}^3$. The best fit to the absorption coefficient and sound velocity are $\Gamma_T = 7.24$ and $c_T = 5.42$, providing relative errors of 4.8% and 3.6% respectively. Figure 2 also shows the relative error in the sound absorption coefficient and sound velocity versus the spatial resolution. Note that the relative error in both quantities also decays roughly like δ^2 which corroborates the second order spatial resolution of the scheme again.

IV. THE EQUILIBRIUM STATE

Within a fluid volume, stress fluctuations arise due to forces involved in the random sequence of molecular collisions. This fluctuating force generates momentum fluctuations. The amplitudes of mass and momentum fluctuations are determined by thermodynamic constraints. Each fluid cell is an open system with constant volume and temperature, in other words, belonging to the grand canonical ensemble. The variance of momentum and

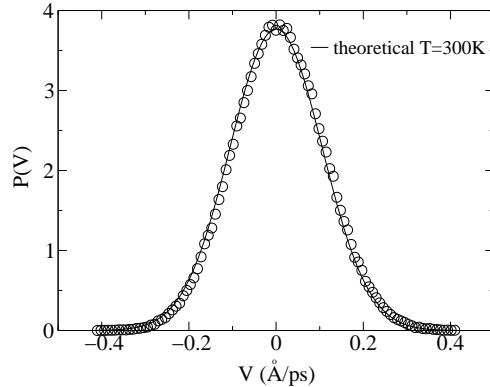


FIG. 4: The equilibrium distribution of the x component of the velocity at one fluid cell of volume 37.5 nm^3 in a simulation of argon (circles) at $T = 300 \text{ K}$ and $\rho = 0.6 \text{ g/mol/\AA}^3$ compared with the theoretical normal distribution (continuum line). In this simulation $\Delta t = 20$ fs and the best normal fit to the numerical distribution yields $T_{num} = 296.28 \text{ K}$, that is a relative error of around 1.2%.

mass of a cell “c” are [1]

$$\begin{aligned}\text{Var}[\mathbf{P}_c \cdot \mathbf{e}] &= \rho V_c k_B T, \\ \text{Var}[M_c] &= \frac{\rho V_c k_B T}{c_T^2},\end{aligned}\quad (13)$$

where \mathbf{e} is a unit surface vector, the mean mass of the cell is ρV_c and c_T is the isothermal sound velocity. On the other hand, these spontaneous mass and momentum fluctuations are transported through the fluid and dissipated following the same mechanism underlying the hydrodynamic modes explained in Appendix A, i.e., either via shear or sound modes.

A. Amplitude of fluctuations

In this section we consider the equilibrium state of argon at different densities (from gas to liquid) and water (TIP3P model, see Appendix B) in order to illustrate that the fluctuations are generated, transported and dissipated in a thermodynamically and hydrodynamically consistent way. First, we confirm that the amplitudes of mass and momentum fluctuations are consistent with thermodynamic relations [1]. In the numerical scheme the amplitude of fluctuations is determined, by construction, via the fluctuation-dissipation theorem [36]. Figure 4 presents a typical distribution of one velocity component and compares it with the theoretical Maxwellian distribution. As usual, a temperature can be extracted from the variance of the velocity distribution. This “numerical” temperature will be labelled as $T_{num} = \sum_{\alpha} \text{Var}[v_{\alpha}] / (3k_B)$.

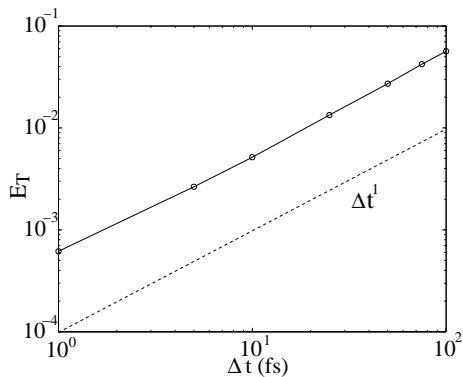


FIG. 5: Relative error in the temperature of the scheme, $E_T = |T_{num} - T|/T$, with $T_{num} \equiv \sum_{\alpha} \text{Var}[v_{\alpha}]/(3k_B)$ and $T = 300$ K the input equilibrium temperature. Results correspond to three-dimensional simulations of water at $\rho = 0.6$ g/mol/Å³ with spatial resolution $\delta = 20$ Å in each direction.

The accuracy of the stochastic time integrator for the Langevin equation affects the value of the numerical temperature. Figure 5 shows the dependence of the relative error in the mean temperature (defined as $E_T = |T_{num} - T_e|/T_e$) with the time step Δt . Good agreement is found and the relative error remains smaller than 10% for $\Delta t \leq 100$ fs.

Figure 6 shows the standard deviation of the cell mass density $\text{Std}[\rho_c]$ against the mean density $\rho = M/V$, where M and V are the total mass and volume of the system. The grand canonical prediction for the equilibrium state is $\text{Std}[\rho] = [\rho k_B T / (c_T^2 V_c)]^{1/2}$ and is compared with the numerical simulations. In the ideal gas limit the sound velocity is just $\sqrt{k_B T / m}$ (with m the molecular mass) and the density fluctuations increase as $\text{Var}[\rho^{(ideal)}] = (m/V)\rho$. As the fluid becomes denser, it becomes less compressible (the isothermal sound speed c_T increases) and as a consequence in the liquid phase the mass fluctuations decrease substantially. Therefore, the largest mass fluctuations are observed at moderate densities (e.g. around $\rho \simeq 0.3$ g/mol/Å³ for argon

see Fig.6). Almost perfect agreement is found between theoretical and numerical results for both argon and water.

B. Correlations at equilibrium

We now show that fluctuations are transported through the system and dissipated in a hydrodynamically correct way. This can be shown via the time correlation of the fluctuating quantities. As shown in Ref. [36], the time correlation of the Fourier components of mass and

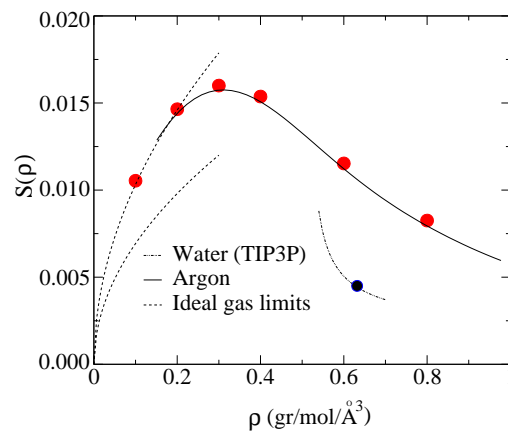


FIG. 6: Standard deviation of the mass density $S[\rho]$ in a fluid cell with volume 37.5 nm³ of argon and water at $T = 300$ K. The continuous line corresponds to the grand canonical results obtained using the equation of state for argon, the dotted lines for water (TIP3P model) $[\rho k_B T / (c_T^2 V_c)]^{1/2}$, and the dashed lines show the ideal gas limits $[(m/V)\rho]^{1/2}$ with $m_{Ar} = 39.498$ g/mol (upper curve) and $m_{H_2O} = 18.015$ g/mol (lower curve). Circles are results from the fluctuating hydrodynamics solver (using a water simulation at $\rho = 0.632$ g/mol/Å³).

momentum satisfy

$$\begin{aligned} \frac{\langle \rho(k, t) \rho(k, 0) \rangle}{\text{Var}[\rho(k, 0)]} &= \exp\{-\Gamma_T k^2 t\} \cos(c_T k t), \\ \frac{\langle g_{\parallel}(k, t) g_{\parallel}(k, 0) \rangle}{\text{Var}[g_{\parallel}(k, 0)]} &= \exp\{-\Gamma_T k^2 t\} \cos(c_T k t), \\ \frac{\langle g_{\perp}(k, t) g_{\perp}(k, 0) \rangle}{\text{Var}[g_{\perp}(k, 0)]} &= \exp\{-\nu k^2 t\}, \\ \frac{\langle \rho(k, t) i g_{\parallel}(k, 0) \rangle}{\langle \rho(k, 0) i g_{\parallel}(k, 0) \rangle} &= \exp\{-\Gamma_T k^2 t\} \sin(c_T k t). \end{aligned} \quad (14)$$

In Eqs.(14) g_{\parallel} indicates the longitudinal momentum, parallel to the wave vector \mathbf{k} , while g_{\perp} indicates the transversal components. Sound modes couple longitudinal momentum and density, as shown in Eqs.(14). According to the Landau description of fluctuating hydrodynamics [1], at a fixed time the stress fluctuations occurring within different fluid volumes are spatially uncorrelated. This means that the variance of the Fourier modes of the hydrodynamic variables ($\text{Var}[\rho(k, 0)] = \langle \rho(k, 0)^2 \rangle$) is independent of the wave-number k . Moreover, fluctuations from the equilibrium state are assumed to be small so that a linear analysis can be applied. This means that perturbations of different wavelengths evolve independently as correlations between fluctuations with different wave-vectors are negligible.

We have evaluated the time correlations of the Fourier components of the hydrodynamic variables in a periodic domain for the set of wave-numbers $k_n = 2\pi n/L$. These correlations were then fitted to the corresponding expo-

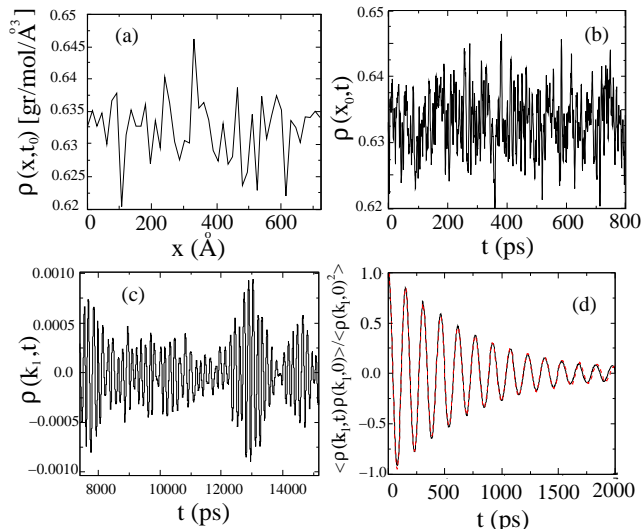


FIG. 7: Water at $\rho = 0.632 \text{ g/mol/\AA}^3$ and $T = 300 \text{ K}$ (ambient conditions) within a periodic box of size $50 \times 50 \times 2250 \text{ \AA}^3$ at equilibrium; the FH mesh is comprised of $1 \times 1 \times 150$ cells. (a) The density field in the real space, $\rho(x, t_0)$. (b) The time-dependence of the density at one cell $\rho(x_0, t)$. (c) The Fourier mode $\rho(k_1, t)$ associated with wavevector $\mathbf{k}_1 = (0, 0, 2\pi/L_z)$. (d) The (normalized) time correlation function $\langle \rho(k_1, t)\rho(k_1, 0) \rangle$. Note the different time scales associated with variations of quantities in (b),(c) and (d). The entire run is of 40 ns duration.

nentially decaying functions of Eqs.(14) to obtain the effective sound frequency $c_T k$ and the effective decay rates for each wave-number (i.e. the inverse of $\Gamma_T k^2$ and νk^2 for sound and shear, respectively). Calculations were done in a periodic system of size $50 \times 50 \times 2250 \text{ \AA}^3$, with a mesh of $1 \times 1 \times 150$ cells, and we considered perturbations with wave-vectors $\mathbf{k}_n = (0, 0, 2\pi n/L_z)$. In order to illustrate the mathematical transformations, Fig.7 shows the density field in the real space $\rho(x, t_0)$ (a), the time-dependence of the density at one cell $\rho(x_0, t)$ (b), the Fourier mode $\rho(k_1, t)$ associated with $k_1 = 2\pi/L_z$ (c) and, finally in (d), the time correlation function $\langle \rho(k_1, t)\rho(k_1, 0) \rangle$ together with the best fit obtained to the theoretical exponential decay of the sound mode. The best fits to the effective decay rates and sound periods for varying wavelength $\lambda_n = 2\pi/k_n$ are compared with the theoretical relations in Fig.8. Note that the theoretical trend agrees quite well with the simulation results for $\lambda > 100 \text{ \AA}$. Considering that the size of one cell in these simulations is 15 \AA , this means that one needs more that about 7 cells to properly resolve one wave. In fact, for wavelengths $\lambda < 100 \text{ \AA}$ the viscosity is underestimated due to the reduction in spatial resolution. The same reasoning applies to the sound time.

V. NON-EQUILIBRIUM STATES

In this section we present standard non equilibrium flow tests performed with the mesoscopic Eulerian solver described in previous sections. In order to do so, firstly we require the description of the explicit boundary conditions for our fluid system enclosed between walls.

A. Boundary conditions

The imposition of boundary conditions on the velocity is illustrated in Fig.9. In the figure the boundary “ w ” is placed at the interface between cells 0 and 1. The fluid region corresponds to cell 0 and continues to the right, while cells 1 and 2 (in grey) are *ghost* cells which are used to impose the desired mechanical behaviour at the boundary “ w ”. In order to close the system, we need to evaluate the momentum flux across the interface w . As at any other cell interface, we approximate $\mathbf{\Pi}_w \cdot \mathbf{e}_w = [(\mathbf{\Pi}_0 + \mathbf{\Pi}_1)/2] \cdot \mathbf{e}_w$, where \mathbf{e}_w is the surface unit vector (in this case \mathbf{e}_{01}). Hence we require knowledge of $\mathbf{\Pi}_1$, the stress tensor in the first *ghost* cell as can also be inferred from Eq. (6) when evaluated at the boundary cell “0”. According to the constitutive relation $\mathbf{\Pi}_1 \propto \nabla \mathbf{v}_1$. Hence, a secondary *ghost* cell (#2 in Fig.9) is required to evaluate the velocity gradient via the central difference scheme: $\nabla v_1 \cdot \mathbf{e}_w = (2\delta)^{-1}(\mathbf{v}_0 - \mathbf{v}_2) \cdot \mathbf{e}_w$ (where δ is the spatial resolution). This closes the set of equations for the velocity at the *ghost* wall cells. This procedure enables certain flexibility: one can either impose the value of the momentum flux $\mathbf{\Pi}_w \cdot \mathbf{e}_w$ (von Neumann boundary condition), a generalized relation involving the fluid velocity at the wall $\mathbf{\Pi}_w \cdot \mathbf{e}_w \propto \mathbf{v}_w$ (Maxwell relation for fluid slip [37]) or the more standard no-slip condition, $\mathbf{v}_w = \mathbf{U}_{wall}$ (Dirichlet boundary condition). In the present work we assume no-slip at the wall and set the velocity of the *ghost* cells accordingly to a linear interpolation of the velocity; with $\mathbf{v}_w = \mathbf{U}_{wall}$ we find

$$\begin{aligned} \mathbf{v}_1 &= 2\mathbf{U}_{wall} - \mathbf{v}_0, \\ \mathbf{v}_2 &= 4\mathbf{U}_{wall} - 3\mathbf{v}_0. \end{aligned} \quad (15)$$

More general slip boundary conditions can be obtained by choosing a different value for \mathbf{v}_w . As is customary, the density at the wall is uniquely controlled by the fluid, meaning that $M_w = M_0 = M_1 = M_2$ [22].

B. Couette, Poiseuille and cavity flows

Stochastic and deterministic simulations for three different flow situations (Couette, Poiseuille and cavity flow) have also been performed, displaying good comparisons with theoretical predictions. Figures 10 and 11 show stationary fluctuating (and deterministic) flows for argon at ambient temperature and mass density $\rho_0 = 0.599 \text{ g/mol/\AA}^3$. The simulations are performed using

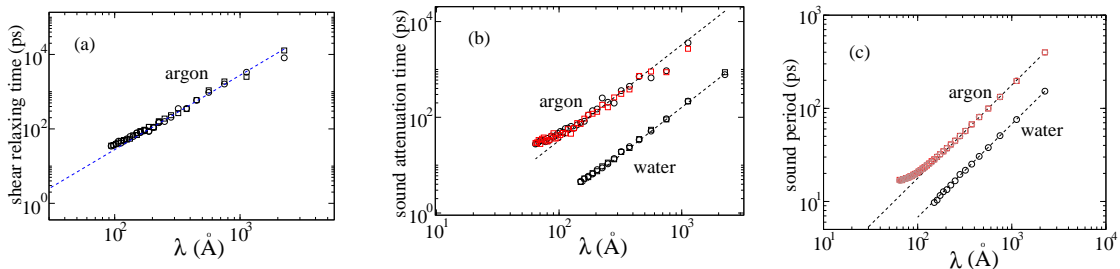


FIG. 8: The best fits to the decay times obtained from the time correlations of the Fourier modes of wavelength $\lambda = 2\pi/k$. Symbols correspond to numerical results and lines to theoretical predictions (see Eqs. (14)). (a) Shear decay times: the lines are the theoretical results $(k^2\nu)^{-1}$, (b) sound attenuation time $(k^2\Gamma_T)^{-1}$ and (c) the sound period λ/c_T . Circles are obtained from the imaginary part of $\langle h(k, \tau)h(k, 0) \rangle$ and squares from the real part, where $h = v_\perp$ (transversal velocity) in (a) while $h = \rho$ in (b) and (c) (similar results, not shown, were obtained for the longitudinal velocity v_\parallel). Results for water ($c_T = 14.75$ Å/ps, $\nu = 84.98$ Å²/ps and $\zeta/\rho = 201.02$ Å²/ps) correspond to the simulations illustrated in Fig.7, while argon ($c_T = 5.61$ Å/ps) corresponds to $\rho = 0.6$ g/mol/Å³ and $T = 300$ K in the same box used in Fig.7.

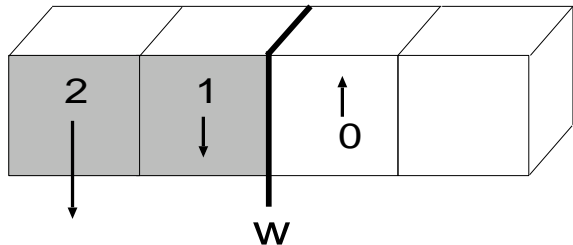


FIG. 9: Boundary conditions imposed at the interface “ w ”. Cell 0 represents a fluid cell, and cells 1 and 2 are *ghost cells*. Arrows indicate the velocity vectors in a case with zero velocity imposed at “ w ” (no-slip boundary condition and rigid wall at rest).

$10 \times 10 \times 10$ cells representing a periodic box of size $200 \times 200 \times 200$ Å³. The fluid is confined in a channel defined by two infinite parallel planes orthogonal to the z axis. In this particular geometry the first two and last two layers of particles in the z direction are *ghost* particles belonging to the walls; the no-slip condition is satisfied at $z_1 = 30$ Å and $z_2 = 150$ Å, so the fluid is confined in a region of width 120 Å.

A Couette flow is shown in Fig.10. We plot the x component of the stationary velocity field in the z direction. The wall amplitude velocity has been set at 2.04 Å/ps, while the amplitude of fluid velocity fluctuations is about 0.5 Å/ps, for the temperature and cell volume considered. The inset picture corresponds to an equivalent simulation but with the thermal fluctuations within the pressure tensor switched off. In this limit, we recover standard Navier-Stokes behaviour.

Figure 11 shows the x component of the stationary velocity field in the z direction for a Poiseuille flow. The applied gravity force in this case is 0.0174 Å/ps². The same simulation performed without thermal fluctuations

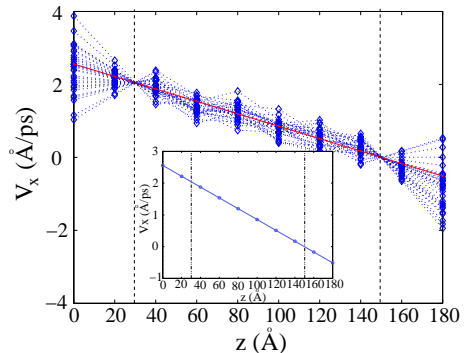


FIG. 10: Stationary Couette profile according to fluctuating hydrodynamics: The diamonds are simulation results and the continuous line is the theoretical stationary linear profile. The wall velocity has been set 2.04 Å/ps. The inset figure shows a deterministic Navier-Stokes simulation with the same parameters. Vertical dashed lines represent the boundary walls.

is displayed in the inset picture and both are compared with the theoretical solution.

We have also carried out simulations of cavity flow for (TIP3P) water depicted in Fig.12 within a domain of dimensions $1500 \times 1500 \times 50$ Å³ and mesh $30 \times 30 \times 1$. The wall is moving at a constant speed of 1 Å/ps in the y direction. The average flow corresponding to averaging the fluctuating hydrodynamics result (Fig. 12b) corresponds to the fluctuation-less flow of Fig. 12a. Although this is quite a large fluid domain, thermodynamic fluctuations are still very visible and have a major effect on the flow. For smaller domains the stationary circulatory flow can be completely nullified by the fluctuations. This kind of cavities can be used as mixers in microfluidics applications, but the extent of the mixing is affected by the magnitude of the fluctuations.

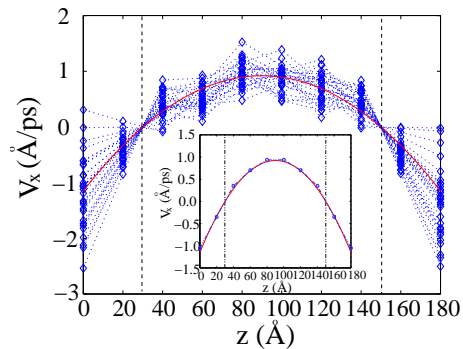


FIG. 11: Stationary Poiseuille profile according to fluctuating hydrodynamics: Diamonds correspond to simulation results and the continuous line is the theoretical profile associated with Navier-Stokes flow. The inset figure shows the same flow case for a purely deterministic simulation. In both figures, the vertical dashed lines represent the walls.

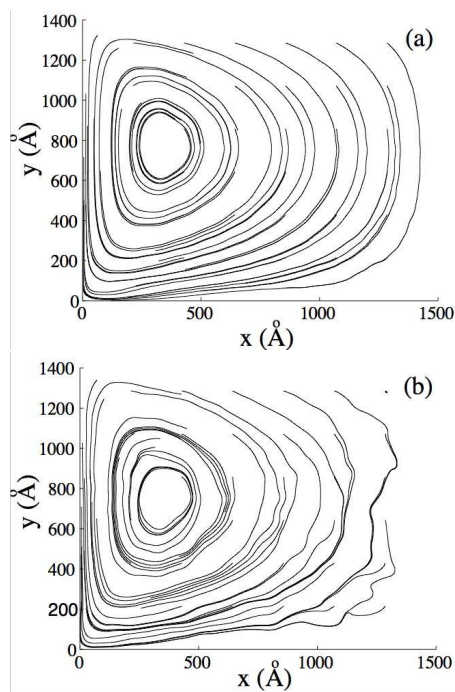


FIG. 12: Streamline plots of a cavity flow for TIP3P water model in the stationary regime. The wall velocity along y is 1 \AA/ps , and the temperature is 300 K . The dimensions of the cavity are $1500 \times 1500 \times 50 \text{ \AA}^3$ and the mesh is $30 \times 30 \times 1$. In (a) thermal fluctuations of the pressure tensors are not present, and the Navier-Stokes solution recovered. In (b) we show the fluctuating hydrodynamics solution.

VI. SUMMARY

We have derived a finite volume discretization of the equations of fluctuating hydrodynamics. The model provides a good representation of the thermodynamic fluc-

tuations which are important at the mesoscale, typically in the nanometer range, as well as the hydrodynamics. We have tested the model in equilibrium and non-equilibrium situations. Simple no-slip boundary conditions have been used and tested in three flow situations Couette, Poiseuille and cavity flow. From a set of molecular dynamics simulations, we have also derived a simple approximation to the equations of state for the TIP3P water model and for argon which permit us to simulate these compressible fluids at ambient temperatures (*ca* 300 K) and pressures around 1 atm .

There are some aspects of the model which could be improved and we reserve for future work. The discretization of the second order derivatives is based on a central difference method. This approach is known to produce instabilities which lead to a characteristic and undesirable alternating pattern in the velocity and density fields [38]. However, we have found that such problems only arise with very strong perturbations well beyond the typical flows at these scales. A further important extension is to incorporate the energy equation so as to be able to model thermal phenomena. Finally, we have used a very simple boundary condition appropriate for the cases studied here: more sophisticated boundary conditions, which may reproduce diverse molecular boundaries (e.g. taking into account the hydrophobic hydrophilic nature of the walls) while also retaining the fluctuations, can be devised in the framework of the hybrid models [4].

Our mesoscopic fluctuating model serves to support a wide range of applications. We are currently using it in hybrid molecular-continuum simulations [4], with implicit solvent models [9], and we plan to use it for the study of microfluidic flows. The use of a regular lattice and the Eulerian description greatly simplify the implementation of this model in a serial (as here) or parallel computing environment. As a result, we believe that it furnishes a unique tool to explore hydrodynamics at the nanoscale including the effects of fluctuations, in stand-alone more or coupled with molecular dynamics.

Acknowledgements

GDF and PVC are grateful to EPSRC (UK) for funding the Integrative Biology project (GR/S72023). MS is supported by the Spanish Ministerio de Educación y Ciencia project FIS2004-01934 and by Programa Propio de Investigación de la UNED (2006). PVC & MS thank EPSRC for funding RealityGrid under grant number GR/R67699, which supported MS's 6 month visit to the CCS at UCL during 2005. RDB acknowledges support from the EU project MERG-CT-2004-006316 and Spanish project CTQ2004-05706/BQU. We are indebted to A. Dejoan, P. Español, E. Flekkoy and S. Succi for helpful discussions.

APPENDIX A: HYDRODYNAMIC MODES

In the isothermal situations the equations that describe the transport of mass and momentum density fields are

$$\begin{aligned}\partial_t \rho &= -\nabla \cdot \mathbf{g}, \\ \partial_t \mathbf{g} &= -\nabla \cdot (\mathbf{g}\mathbf{v}) - \nabla p + \eta \nabla^2 \mathbf{v} + \left(\frac{\eta}{3} + \zeta\right) \nabla (\nabla \cdot \mathbf{v}).\end{aligned}\quad (\text{A1})$$

The equilibrium state is characterized by a constant density field ρ_e and a zero momentum density field $\mathbf{g}_e = 0$ because the fluid is at rest. For fluctuations of small enough amplitude, the relaxation towards equilibrium is governed by the linearized version of the mass and momentum Eqs.(A1). By decomposing the hydrodynamic fields as $\rho(\mathbf{r}, t) = \rho_e + \delta\rho(\mathbf{r}, t)$ and $\mathbf{g}(\mathbf{r}, t) = \delta\mathbf{g}(\mathbf{r}, t)$, the linearized version of Eqs.(A1) for the perturbations results

$$\begin{aligned}\partial_t \delta\rho &= -\nabla \cdot \delta\mathbf{g}, \\ \partial_t \delta\mathbf{g} &= -\nabla p + \nu \nabla^2 \delta\mathbf{g} + \nu_B \nabla (\nabla \cdot \delta\mathbf{g}),\end{aligned}\quad (\text{A2})$$

with the usual definitions for the kinematic shear viscosity $\nu \equiv \eta/\rho_e$ and the effective bulk viscosity $\nu_B \equiv (\eta/3 + \zeta)/\rho_e$.

Under isothermal conditions the thermodynamic relation of pressure perturbation δp with density and temperature becomes simply [39],

$$\delta p(\rho, T) = c_T^2(\rho) \delta\rho, \quad (\text{A3})$$

where $c_T^2 \equiv (\partial p/\partial \rho)_T$ is the squared isothermal sound velocity.

Let us consider a general solution as a series of normal modes

$$\mathbf{a}(\mathbf{r}, t) = \mathbf{a}(\mathbf{k}, t) e^{i\mathbf{k} \cdot \mathbf{r}},$$

where we have gathered the hydrodynamic variables in the array $\mathbf{a} = \{\delta\rho, \delta\mathbf{g}\}$. Taking the Fourier transform in Eqs. (A2) one gets the equations $\mathbf{a}(\mathbf{k}, t)$. In the linear regime there is no coupling between modes and without loss of generality one can work in the reference system for which the wave vector is $\mathbf{k} = (k, 0, 0)$,

$$\frac{d\mathbf{a}(k, t)}{dt} = \mathbf{H}\mathbf{a}(k, t) \quad (\text{A4})$$

where $\mathbf{a}(k, t) = (\rho(k, t), g_x(k, t), g_y(k, t), g_z(k, t))^T$ and the hydrodynamic matrix is

$$\mathbf{H} \equiv - \begin{bmatrix} 0 & ik & 0 & 0 \\ ic_T^2 k & \nu_L k^2 & 0 & 0 \\ 0 & 0 & \nu k^2 & 0 \\ 0 & 0 & 0 & \nu k^2 \end{bmatrix}, \quad (\text{A5})$$

with the kinematic longitudinal viscosity defined as $\nu_L = \nu + \nu_B$. The eigenvalues of the hydrodynamic matrix

\mathbf{H} provide the growth rates of the normal modes of the system given by Eq. (A4). The eigenvalues are obtained from the roots of the characteristic equation $\det[\mathbf{H} - \omega \mathbf{1}] = 0$, which results in

$$(\omega + \nu k^2)^2 (\omega^2 + \nu_L k^2 \omega + c_T^2 k^2) = 0. \quad (\text{A6})$$

The solutions are

$$\begin{aligned}\omega_{1,2} &= -\nu k^2, \\ \omega_{3,4} &= -\Gamma_T k^2 \pm i s_T k,\end{aligned}\quad (\text{A7})$$

where we have defined Γ_T as the isothermal sound absorption coefficient and s_T as the sound speed depending on the wave vector given by

$$\begin{aligned}\Gamma_T &= \frac{\nu_L}{2}, \\ s_T &= \frac{\sqrt{4c_T^2 - \nu_L^2 k^2}}{2}.\end{aligned}\quad (\text{A8})$$

The first two eigenvalues ($\omega_{1,2}$) correspond to the two shear modes associated with the exponential decay of the transversal momentum g_y and g_z . Sound modes correspond to $\omega_{3,4}$. Indeed, as can be seen from Eqs. (A7) and Eqs. (A8), sound is underdamped if s_T is a real number. However, according to Eq. (A8) if $k > 2c_T/\nu_L$, sound becomes overdamped. Nevertheless for most liquids $c_T/\nu_L \sim O(1)$ so this anomalous solution occurs at quite small wavelengths for which the present mesoscopic description does not apply (at molecular lengthscales one should consider the dependence of the transport coefficients on k within the generalized hydrodynamic formalism [39]). As a matter of fact, the difference between s_T and c_T is negligible for any mesoscopic wavelength, so throughout the present paper we assume that $s_T = c_T$.

With this last approximation, the solution is given by

$$\begin{aligned}\rho(\mathbf{k}, t) &= \rho_e + \rho(\mathbf{k}, 0) \exp\{-\Gamma_T k^2 t\} \cos(c_T k t) \\ &\quad - \frac{i}{c_T} \exp\{-\Gamma_T k^2 t\} \sin(c_T k t) \hat{\mathbf{k}} \cdot \mathbf{g}(\mathbf{k}, 0), \\ \mathbf{g}(\mathbf{k}, t) &= \exp\{-\Gamma_T k^2 t\} [\cos(c_T k t) \hat{\mathbf{k}} \cdot \mathbf{g}(\mathbf{k}, 0) \\ &\quad - i \sin(c_T k t) c_T \rho(\mathbf{k}, 0)] \hat{\mathbf{k}} \\ &\quad + \exp\{-\nu k^2 t\} (\mathbf{1} - \hat{\mathbf{k}} \hat{\mathbf{k}}) \cdot \mathbf{g}(\mathbf{k}, 0)\end{aligned}\quad (\text{A9})$$

where $\hat{\mathbf{k}} = \mathbf{k}/|\mathbf{k}|$ is the unit wave vector.

APPENDIX B: EQUATIONS OF STATE FOR ARGON AND WATER VIA MOLECULAR DYNAMICS SIMULATION

In this section we study the equations of state for water and also argon through molecular dynamic simulations using the NAMD molecular dynamics code [40]. In particular, the theoretical Lennard-Jones equation of state for argon given in Refs.[30, 31, 32] is not necessarily exact because our MD simulations using the CHARMM

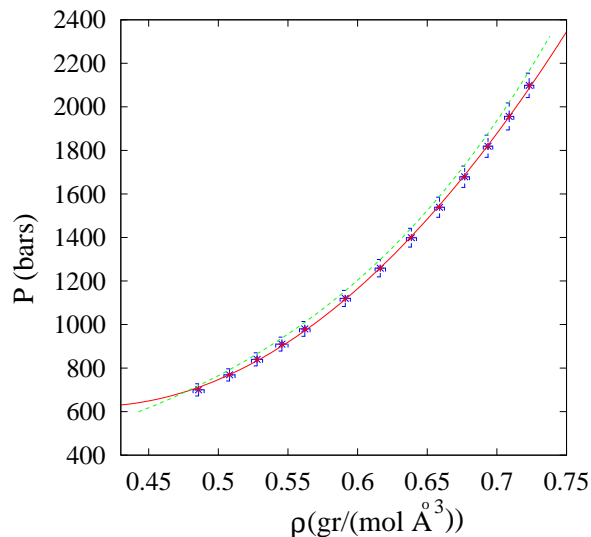


FIG. 13: Argon equation of state: Pressure (in bars) versus mass density at temperature 300K. The simulation results appear with error bars and the dashed line is the equation of state for the theoretical Lennard-Jones fluid in Ref.[30, 31, 32]. The continuous line is the fit of the numerical data to the second order polynomial $3088.21 - 12065.2\rho + 14765.8\rho^2$.

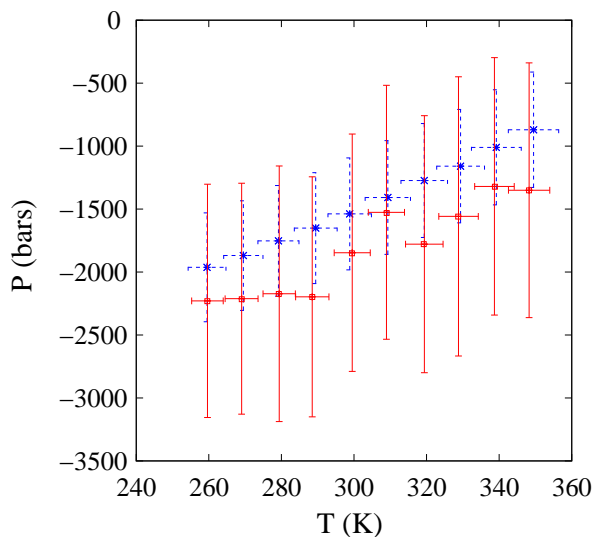


FIG. 14: Water pressure (in bars) versus temperature obtained from MD simulations of the TIP3P water model (using NAMD) at a fixed density $\rho = 0.55066 \text{ g}/(\text{mol } \text{Å}^3)$. The * symbols correspond to simulations with all bonds rigid while the \square symbols are for non rigid bonds.

force field perturb the Lennard-Jones potential close to the cutoff radius, smoothing it to zero [40]. Thus we decided to obtain an accurate approximation of the equation of state by directly fitting the data obtained from molecular dynamics simulations to a second order polynomial. These considerations also apply for the TIP3P water model.

We have computed the equation of state for argon in our molecular model in the NpT ensemble at a fixed temperature $300 \pm 4 \text{ K}$ with 5000 argon atoms. The simulations are performed with a time step $\Delta t = 1 \text{ fs}$. We have made use of a switched Lennard-Jones potential [40] between 10 and 12 Å. The results are displayed in Fig.13 for the mass density. Note that the deviations between the theoretical model and the simulation results for the pressure can be as large as 15% in the units presented in the graph, the simulated argon pressure always being less than that given by the theoretical Lennard-Jones equation of state in Ref.[30, 31, 32].

Concerning the water equation of state, we have performed simulations of water molecules using the TIP3P water model [2]. In Fig.14 we present the simulation results for a range of temperatures around 300K with a time step $\Delta t = 1 \text{ fs}$. We have chosen a fixed density $\rho = 0.55066 \text{ g}/(\text{mol } \text{Å}^3)$ what gives (in a NVT ensemble for a cubic periodic box of size 30 Å) a total of 826 water molecules. We have also tested the effect of using rigid bonds. We see that for harmonic bonds the fluctuations in pressure are bigger compared to those of the rigid simulation providing also smaller mean average pressures in general terms. We have also compared our results with three analytical models for the water equation of state presented in Ref. [33]. We observe clear deviations from the models. Basically, all three theoretical models largely overestimate the isothermal sound velocity at any value of the density considered. This reinforces the necessity of pre-calibrating the equation of state for each particular fluid considered; for instance via MD simulations as done here.

In Fig.15 we plot the values of mass densities obtained from water MD simulations in an NpT ensemble against pressure (in bars) at a fixed temperature $300 \pm 5 \text{ K}$ with non-rigid water molecules and a time step $\Delta t = 1 \text{ fs}$. The second order polynomial fit used in the FH equations is also shown in the continuous line.

-
- [1] L. D. Landau and E. M. Lifshitz, *Fluid mechanics* (Pergamon Press, New York, 1959).
 [2] W. Jorgensen, J. Chandrasekhar, J. Madura, R. Impey, and M. Klein, *J. Chem. Phys.* **79**, 926 (1983).
 [3] R. Delgado-Buscalioni and P. V. Coveney, *Phys. Rev. E*

- 67**, 046704 (2003).
 [4] G. De Fabritiis, R. Delgado-Buscalioni, and P. V. Coveney, *Phys. Rev. Lett.* **97**, 134501 (2006).
 [5] R. Delgado-Buscalioni, E. Flekkøy, and P. V. Coveney, *Europhys. Lett.* **69**, 959 (2005).

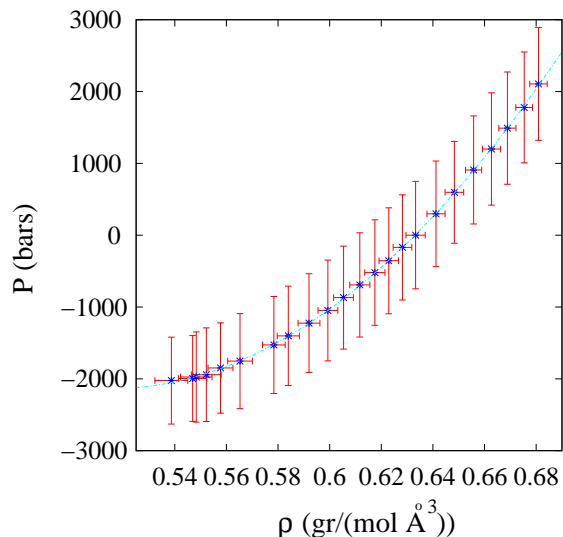


FIG. 15: Water pressure (in bars) versus mass density for a temperature of 300 K from MD simulations of the non-rigid TIP3P water model (results obtained with the NAMD code). The continuous line is the best fit of the numerical data to the second order polynomial $p(\rho) = 38373.6 - 157398\rho + 152881\rho^2$ bars.

- [6] P. V. Coveney, G. De Fabritiis, M. Harvey, S. Pickles, and A. Porter, *Comp. Phys. Comm.* **175**, 389 (2006).
- [7] J. Atencia and D. J. Beebe, *Nature* **437**, 648 (2005).
- [8] P. Ahlrichs and B. Dunweg, *J. Chem. Phys.* **111**, 8225 (1999).
- [9] G. De Fabritiis, G. Giupponi, and P. V. Coveney, preprint (2006).
- [10] P. Español, *Trends in Nanoscale Mechanics: Analysis of Nanostructured Materials and Multi-Scale Modeling* (V. M. Harik and M. D. Salas editors (Kluwer), 2003).
- [11] S. Succi, *The Lattice Boltzmann Equation for Fluid Dynamics and Beyond* (Oxford University Press, 2001).
- [12] A. Malevanets and R. Kapral, *J. Chem. Phys.* **110**, 8605 (1999).
- [13] P. J. Hoogergrugge and J. M. V. A. Koelman, *Europhys. Lett.* **19**, 155 (1992).
- [14] P. Español and P. Warren, *Europhys. Lett.* **30**, 191 (1995).
- [15] R. Benzi, S. Succi, and M. Vergassola, *Phys. Rep.* **222**, 145 (1992).
- [16] S. S. Chikatamarla and I. V. karlin, *Phys. Rev. Lett.* **97**, 190601 (2006).
- [17] F. J. Higuera, S. Succi, and R. Benzi, *Europhys. Lett.* **9**, 345 (1989).
- [18] S. Succi, O. Filippova, G. Smith, and E. Kaxiras, *Computing in Science and Engineering* **03**, 26 (2001).
- [19] O. B. Usta, A. J. C. Ladd, and J. E. Butler, *J. Chem. Phys.* **122**, 094902 (pages 11) (2005).
- [20] A. J. C. Ladd, *J. Fluid Mech.* **271**, 331 (1994).
- [21] R. Adhikari, K. Stratford, M. E. Cates, and A. J. Wagner, *Europhys. Lett.* **71**, 473 (2005).
- [22] A. L. Garcia, M. M. Mansour, G. C. Lie, and E. Clementi, *J. Stat. Phys.* **47**, 209 (1987).
- [23] M. Serrano and P. Español, *Phys. Rev. E* **64**, 046115 (2001).
- [24] M. M. Mansour, A. L. Garcia, G. C. Lie, and E. Clementi, *Phys. Rev. Lett.* **58**, 874 (1987).
- [25] H. C. Öttinger, *Phys. Rev. E* **57**, 1416 (1998).
- [26] E. G. Flekkøy, P. V. Coveney, and G. De Fabritiis, *Phys. Rev. E* **62**, 2140 (2000).
- [27] P. E. Kloeden and E. Platen, *Numerical solution of stochastic differential equations* (Springer-Verlag, Berlin, 1992).
- [28] G. De Fabritiis, M. Serrano, P. Español, and P. V. Coveney, *Physica A* **361**, 429 (2006).
- [29] M. Serrano, G. De Fabritiis, P. Español, and P. V. Coveney, *Math. Comput. Simulat.* **72**, 190 (2006).
- [30] K. Johnson, J. A. Zollweg, and K. E. Gubbins, *Mol. Phys.* **78**, 591 (1993).
- [31] D. M. Heyes, *Chem. Phys. Lett.* **153**, 319 (1988).
- [32] P. Borgelt, C. Hoheisel, and G. Stell, *Phys. Rev. E* **42**, 789 (1990).
- [33] C. Jeffrey and P. Austin, *J. Chem. Phys.* **110**, 484 (1999).
- [34] G. Guo and Y. Zhang, *Mol. Phys.* **99**, 283 (2001).
- [35] M. Grmela and H. C. Öttinger, *Phys. Rev. E* **56**, 6620 (1997).
- [36] J. Keizer, *Statistical thermodynamics of nonequilibrium processes* (Springer-Verlag, New York, 1987).
- [37] C. Neto, D. R. Evans, E. Bonaccorso, H.-J. Butt, and V. S. J. Craig, *Reports on Progress in Physics* **68**, 2859 (2005).
- [38] S. V. Patankar, *Numerical heat transfer and fluid flow* (Taylor&Francis, 1980).
- [39] J. P. Boon and S. Yip, *Molecular Hydrodynamics* (McGraw Hill, New York, 1980).
- [40] J. C. Phillips, R. Braun, W. Wang, J. Gumbart, E. Tajkhorshid, E. Villa, C. Chipot, R. D. Skeel, L. Kalé, and K. Schulten, *J. Comp. Chem.* **26**, 1781 (2005).